

Study on the Aerodynamic Performance of Novel Bypass Shock-Induced Thrust Vector Nozzle

K. Wu¹, Z. Liu¹, R. Deng², G. Zhang¹, Z. Zhu¹, V. R. P. Sethuraman³ and X. Su^{1,†}

¹Key Laboratory of Fluid Transmission Technology of Zhejiang Province, Zhejiang Sci-Tech University, Hangzhou, Zhejiang Province, 310018, China

²Department of Control Science and Engineering, Tongji University, Shanghai, 200092, China

³Department of Aerospace System Engineering, Sejong University, Seoul, 05006, South Korea

†Corresponding Author Email: suxianghui@sina.com

(Received September 11, 2022; accepted December 12, 2022)

ABSTRACT

This article studies the aerodynamic performance of a novel bypass shock-induced thrust vector nozzle. An arc-shaped bypass is innovatively designed to optimize nozzle performance and equips a variable shrinkage part. The nozzle performance is investigated numerically under diverse shrinkage area ratios. Computational results indicate that both geometry and friction choking have important effects on the nozzle performance. Normally, in the case of without any bypass shrinkage, the flow choking occurs at the bypass outlet. Very small bypass shrinkage is unable to change the flow choking location. The bypass geometry choking comes up at its throat as the shrinkage area ratio of the bypass reaches 0.06. According to computational results, the vectoring angle diminishes with the increasing shrinkage area ratio of the bypass, thrust force ratio, thrust efficiency, specific impulse ratio, and coefficient of discharge increase. As the NPR enlarges, the deflection angle and thrust efficiency decrease, and the thrust force ratio increases.

Keywords: Aerodynamics; Aeronautics; Supersonic nozzle; Shock-induced thrust vector control; Flow control.

NOMENCLATURE

A	area	P_0	total pressure
A_{br}	bypass throat area	P_b	back-pressure
A_e	exit area	P_e	area-weighted average pressure on nozzle exit plane
A_t	nozzle throat area	P_{uw}	static pressure on the top wall
C_D	coefficient of discharge	R_1	transitional arc radius
C_E	thrust efficiency	R_2	internal arc radius
C_F	thrust force ratio	R_3	external arc radius
F_h	horizontal force	R_4	throat transition radius
$F_{i,b}$	ideal bypass thrust	R_e	Reynolds number
$F_{i,p}$	ideal mainstream thrust	R_g	specific gas constant
r	real thrust	T_0	total temperature
F_s	safety factor	U_{ex}	horizontal velocity
F_v	vertical force	U_{ey}	vertical velocity
H_1	inlet height	X	axial distance
H_b	bypass height	X_a	horizontal coordinate of the left starting point on the variable part
H_{br}	bypass throat height	X_b	horizontal coordinate of the right ending point on the variable part
H_e	exit height	X_i	horizontal coordinate of any point on the variable part
H_t	nozzle throat height	Y_a	vertical coordinate of the left starting point on the variable part
i	normalized coordinate	Y_b	vertical coordinate of the right ending point on the variable part
$I_{i,sp}$	theoretical specific impulse		
I_{sp}	actual specific impulse		
K	specific impulse coefficient		
L_1	distance between the original point and the bypass inlet		
L_2	distance between the original point and		

	the nozzle throat	Y_i	vertical coordinate of any point on the variable part
L_3	distance between the original point and the straight diverging part	ζ	bypass mass flow ratio
L_4	distance between the original point and the arc bypass center	γ	specific heat ratio ($\gamma = 1.4$ for air)
L_5	nozzle length	ρ	density
L_{c-d}	length of the converging-diverging part of the nozzle	δ_v	vectoring angle
L_d	length of the diverging part of the nozzle	θ	diverging angle of the Laval nozzle
\dot{m}	bypass mass flow rate	2-D	two-dimensional
\dot{m}_b	actual bypass mass flow rate	3-D	three-dimensional
$\dot{m}_{i,b}$	ideal bypass mass flow rate	AR	area ratio
\dot{m}_p	actual mass flow rate for the Laval nozzle	GCI	Grid Convergence Index
N	refinement ratio	LES	Large Eddy Simulation
		NPR	Nozzle Pressure Ratio
		PUV	Primary Upstream Vortex
		SPR	Secondary Pressure Ratio
		SUV	Secondary Upstream Vortex

1. INTRODUCTION

Thrust vector control (TVC) is achieved through the thrust vector nozzle (TVN). It includes two major categories: mechanical TVN (MTVN) and fluidic TVN (FTVN) (Wu *et al.* 2020b; Wu and Kim 2021). MTVN is reliable (Sung and Hwang 2004; Kong *et al.* 2016; Cong *et al.* 2019; Wu 2022), however, many mechanical types of equipment result in a series of problems, such as wear and overweight (Chouicha *et al.* 2020). FTVN can effectively resolve these technical issues (Burcham *et al.* 1990; Das *et al.* 2016). FTVN includes counter-flow TVN (Wu *et al.* 2018, 2019a; Wu and Kim 2019a), co-flow TVN (Heo and Sung 2012), throat-shifting TVN (TSTVN) (Deere 2003; Deere *et al.* 2003), dual-throat TVN (DTTVN) (Ferlauto and Marsilio 2016; Wu and Kim 2019b), bypass DTTVN (BDTTVN) (Wang *et al.* 2019), shock-induced TVN (SITVN), and bypass SITVN (BSITVN).

Waithe and Deere (2003), Wu and Kim (2019a, c), and Wu *et al.* (2019a, 2020c) experimentally, theoretically, and numerically analyzed the performance of rectangular SITVN using a slot injector, and clarified that nozzle pressure ratio (NPR), injection angle, and position and aspect ratio of the slot affect its performance significantly. Zmijanovic *et al.* (2012, 2014, 2016), Zou and Wang (2011), and Sellam *et al.* (2015) conducted analytical, computational, and experimental research on control effectiveness of the hole injector for conical SITVN, and expounded the impacts of hole location, NPR, and type of gas on the nozzle performance. Since a heavy chamber is essential to offer the secondary flow for a traditional SITVN, an easier bypass SITVN is designed and developed in recent years. It further simplifies the structure of SITVN remarkably, eliminates the heavyweight chamber, and adopts a fairly light bypass.

Deng and Kim (2015) conducted two-dimensional (2-D) numerical simulations on the steady-state flow field of a BSITVN and illuminated that NPR and injection port impact the nozzle performance significantly. Bhattacharya and Ahmed (2010), Joshi and Bhattacharya (2019), and Bhattacharya and Gregory (2020) investigated the cylinder wake

with a 3-D disturbance and shedding for diverse Reynolds numbers, obtained the detailed evolution of the wake vortex, and explained the differences between active and passive flow control. Deng *et al.* (2016) further conducted simulations based on the LES method and demonstrated that the vectoring deflection can be properly controlled while the bypass mass flow ratio is less than 7%. Islam *et al.* (2018a,b) carried out 3-D computational studies on steady-state features of the BSITVN for NPR = 2.4 and a constant bypass mass flow ratio of 4.9%. They compared two kinds of bypass widths (20% and 75% widths along the spanwise direction) and elaborated that the internal shock structure varies significantly with the formation of a flow separation region near the bypass outlet.

So far, an essential issue is unsolved for BSITVN. It is a kind of passive control method. Once the nozzle design is determined, the vectoring performance can only be achieved by changing the NPR. The variation of NPR may lead to over-expanded, fully expanded, and under-expanded conditions. Therefore, the current work carries out an active bypass flow modulation. Bhattacharya and Gregory (2015a, b, 2018), and Bhattacharya and Ahmed (2020) investigated the 3-D forcing of the cylinder wake, implemented spanwise-modulated DBD plasma actuators for flow control, and pointed out the advantages of active flow control.

Earlier investigations of the BSITVN with the N-shaped bypass have a shortcoming. As shown in Fig. 1(a), two elbows lead to uncertainty of the bypass flow choking and the formation of separation bubbles for various downstream pressure situations (Islam *et al.* 2018a, b). Hence, some errors may occur in calculating the bypass mass flow rate. To make up for the deficiencies above, a brand-new arc bypass is developed, as shown in Fig. 1(b). Furthermore, another circular transition part between the arc bypass and the combustor is optimized to eliminate the formation of separation bubbles near the bypass inlet. At the top part of the bypass, a variable shrinkage part is used to adjust the bypass mass flow rate accurately. The influences of different shrinkage ratios of the bypass and NPR on the system's performance are

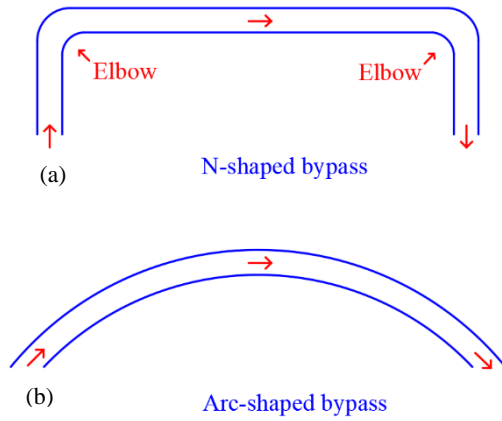


Fig. 1. Comparison between traditional N-shaped bypass and new arc-shaped bypass (a) N-shaped bypass; (b) arc-shaped bypass.

investigated for a profound understanding of the BSITVN.

2. MECHANISM OF BYPASS SHOCK-INDUCED THRUST VECTOR NOZZLE

The BSITVN adopts an effective principle to control the vectoring deflection. Figure 2 depicts a simplified sketch of the BSITVN. The mainstream goes through the Laval nozzle, and the secondary flow passes through the arc bypass. The subsonic mainstream ($M < 1$) accelerates in the converging part of the Laval nozzle until it reaches the choking

state ($M=1$) at its throat and further accelerates in the diffusion part. Based on the Fanno flow theory, the bypass flow through the channel accelerates and is eventually blocked at the bypass outlet (Zucker and Biblarz 2002). Two independent separation zones filled with rotating vortices form. The anticlockwise rotating primary upstream vortex (PUV) determines the smooth pressure increment, and the clockwise rotating secondary upstream vortex (SUV) determines the pressure variation near the bypass outlet. The separation shock collides with the bow shock and merges into a strong incident shock. In consequence, the jet deflection with an angle of δ_v is achieved, as depicted in Eq. (1) (Zmijanovic *et al.* 2012, 2014, 2016).

$$\delta_v = \tan^{-1}(F_v / F_h) \quad (1)$$

The vertical thrust force F_v and horizontal thrust force F_h can be calculated according to Eq. (2) and Eq. (3), respectively.

$$F_v = (\dot{m}_b + \dot{m}_p) \cdot U_{ey} \quad (2)$$

$$F_h = (\dot{m}_b + \dot{m}_p) \cdot U_{ex} + (P_e + P_b) \cdot A_e \quad (3)$$

Other core performance factors are also defined to evaluate the BSITVN, including bypass mass flow ratio, ζ , thrust force coefficient, C_F , thrust efficiency, C_E , specific impulse coefficient, K , and coefficient of discharge, C_D (Sellam *et al.* 2015; Zmijanovic *et al.* 2016).

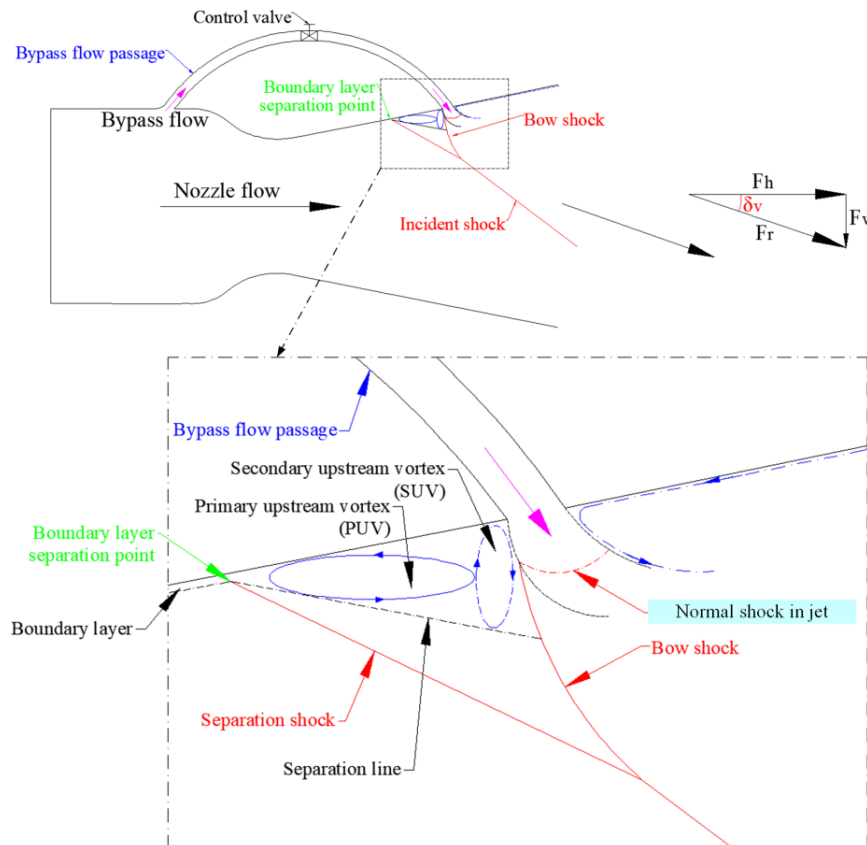


Fig. 2. Simplified flow field sketch of the new BSITVN.

The bypass mass flow ratio, ζ , defines a ratio between the bypass flow and the incoming flow from the combustor, which can be expressed in Eq. (4).

$$\zeta = \frac{\dot{m}_b}{\dot{m}_b + \dot{m}_p} \quad (4)$$

The thrust force ratio is defined as follows:

$$C_F = \frac{F_r}{F_i} = \frac{\sqrt{F_h^2 + F_v^2}}{F_{i,p} + F_{i,b}} \quad (5)$$

$$F_{i,p} = \dot{m}_p \sqrt{\frac{2\gamma R_g T_0}{\gamma - 1} \left[1 - \left(\frac{P_b}{P_0} \right)^{\frac{\gamma-1}{\gamma}} \right]} \quad (6)$$

$$F_{i,b} = \dot{m}_b \sqrt{\frac{2\gamma R_g T_0}{\gamma - 1} \left[1 - \left(\frac{P_b}{P_0} \right)^{\frac{\gamma-1}{\gamma}} \right]} \quad (7)$$

The thrust efficiency, C_E , is calculated by Eq. (8).

$$C_E = \frac{|\delta_v|}{\left(\frac{\dot{m}_b}{\dot{m}_b + \dot{m}_p} \right) * 100} \quad (8)$$

The specific impulse coefficient, K , shows the ratio of the actual specific impulse, I_{sp} , and theoretical specific impulse, $I_{i,sp}$, which is shown in Eq. (9).

$$K = \frac{I_{sp}}{I_{i,sp}} = \frac{\sqrt{F_h^2 + F_v^2} / (\dot{m}_p + \dot{m}_b)}{(F_{i,p} + F_{i,b}) / (\dot{m}_{i,p} + \dot{m}_{i,b})} \quad (9)$$

Since both the Laval nozzle and bypass are choked, the ideal mass flow rates through them can be calculated based on Eq. (10) and Eq. (11).

$$\dot{m}_{i,p} = \frac{A_r P_0}{\sqrt{T_0}} \sqrt{\frac{\gamma}{R_g}} \left(\frac{\gamma + 1}{2} \right)^{-\frac{\gamma+1}{2(\gamma-1)}} \quad (10)$$

$$\dot{m}_{i,b} = \frac{A_b P_0}{\sqrt{T_0}} \sqrt{\frac{\gamma}{R_g}} \left(\frac{\gamma + 1}{2} \right)^{-\frac{\gamma+1}{2(\gamma-1)}} \quad (11)$$

The coefficient of discharge, C_D , is the ratio of actual discharge to the theoretical one, which is expressed in Eq. (12).

$$C_D = \frac{\dot{m}_r}{\dot{m}_i} = \frac{\dot{m}_b + \dot{m}_p}{\dot{m}_{i,b} + \dot{m}_{i,p}} \quad (12)$$

3. NUMERICAL APPROACH

3.1 Governing Equation

The RANS equation in 2-D, steady-state and compressible flow is solved. Corresponding mass, momentum, and energy equations can be written as follows:

$$\nabla \cdot (\rho \vec{v}) = 0 \quad (13)$$

$$\nabla \cdot (\rho \vec{v} \vec{v}) = \nabla \cdot (\vec{\tau}) - \nabla p \quad (14)$$

$$\nabla \cdot \left(\rho \vec{v} \left(e + \frac{v^2}{2} \right) \right) = \nabla \cdot (\vec{\tau} \cdot \vec{v}) - \nabla \cdot (\rho \vec{v}) \quad (15)$$

3.2 Geometry

Figure 3 shows the geometry model and Table 1 gives detailed dimensions. The basic geometry except for the arc bypass is cited from the experimental work done by [Waithe and Deere \(2003\)](#). The arc bypass is put forward based on the

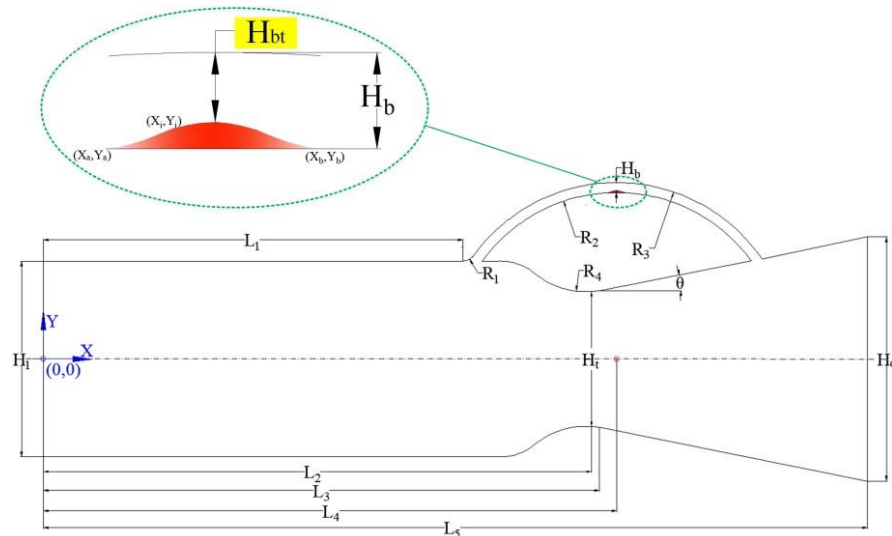


Fig. 3. Geometry model of the BSITVN.

Table 1 Geometry parameters of the BSITVN

Parameters	Value
Nozzle inlet height, H_I	40 mm
Bypass height, H_b	2.032 mm
Nozzle throat height, H_t	27.48 mm
Nozzle exit height, H_e	49.38 mm
Distance between original point and bypass inlet, L_1	85.65 mm
Distance between original point and nozzle throat, L_2	110.6 mm
Distance between original point and straight diverging part, L_3	113.6 mm
Distance between original point and arc bypass center, L_4	117.123 mm
Nozzle length, L_5	168.367 mm
Radius of transition arc, R_1	2.83 mm
Internal arc radius, R_2	34 mm
External arc radius, R_3	36.032 mm
Radius of nozzle throat transition, R_4	15.89 mm
Diverging angle, θ	11.01°

optimization of earlier research considering N-shaped bypasses (Deng and Kim 2015; Deng *et al.* 2016; Islam *et al.* 2018a, b). Two significant advantages of this kind of arc bypass are available. One of the advantages is that it is a very simple and active control technology for actual engineering applications. Another advantage is easy to predict the bypass choking location.

The throat and exit height of the Laval nozzle is $H_t = 27.48$ mm and $H_e = 49.38$ mm, respectively. The

diverging angle is $\theta = 11.01^\circ$. The connection part between the Laval nozzle and bypass inlet has an arc transition port of $R_1 = 2.83$ mm. It can avoid the occurrence of recirculation bubbles in the bypass inlet effectively. The height of the arc bypass is $H_b = 2.032$ mm, in which the radiuses of the inner and outer arc lines are $R_2 = 34$ mm and $R_3 = 36.032$ mm. The distance from the center of the two arcs to the origin is $L_4 = 117.123$ mm. The basic reference case that has a constant area bypass is replaced by adding a shrinkage section. The abscissa and ordinate of any point (X_i, Y_i) on the variable arc line follow Eq. (16) and Eq. (17), respectively.

$$X_i = (1-i) \cdot X_a + i \cdot X_b, \quad 0 \leq i \leq 1 \quad (16)$$

$$Y_i = \sqrt{34^2 - (X_i - 117.123)^2} + 0.5 \cdot (H_b - H_{bt}) \cdot [1 - \cos(2\pi i)] \quad (17)$$

where i is normalized horizontal coordinate; among them, $[X(0), Y(0)] = [X(a), Y(a)]$ and $[X(1), Y(1)] = [X(b), Y(b)]$.

In this article, eight shrinkage area ratios of the bypass are studied for NPR = 4.6, including AR = 0, 0.05, 0.06, 0.08, 0.1, 0.4, 0.7, and 0.9. Subsequently, different NPR values are investigated for AR = 0.4 to explore how NPR changes affect aerodynamic performance.

3.3 Domain and Boundary Conditions

Figure 4 depicts the overall domain as well as the grid division and appropriate boundary conditions.

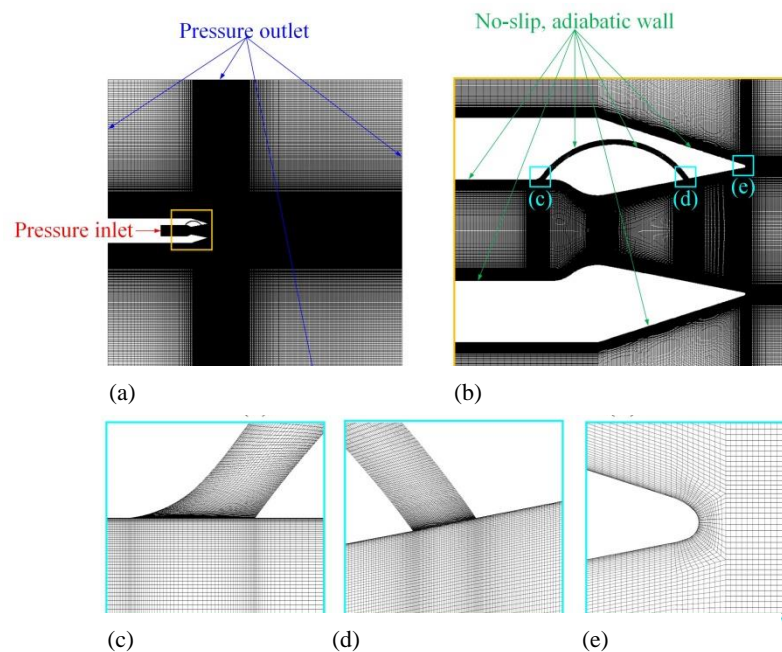


Fig. 4. Computational mesh and boundary conditions (a) full domain; (b) partial region; (c) bypass inlet; (d) bypass exit; (e) upper wall exit region.

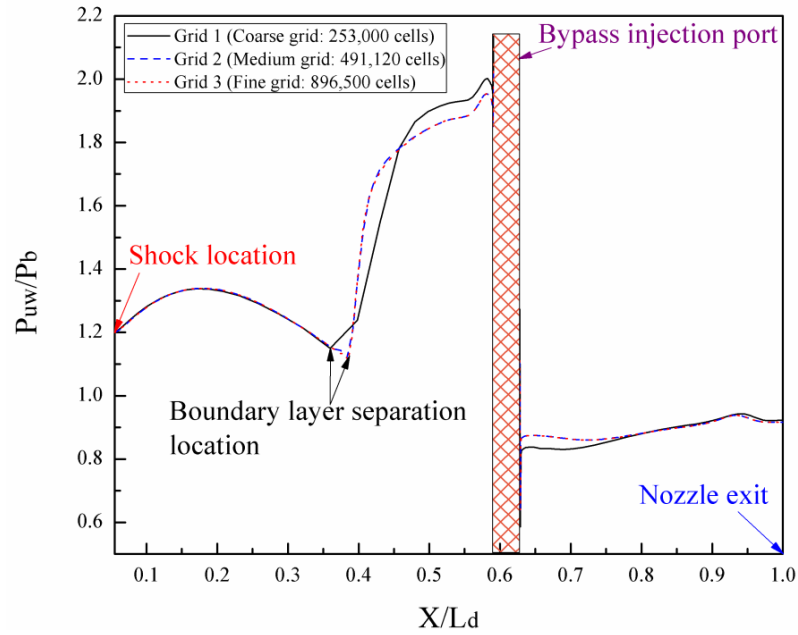


Fig. 5. Static pressure distributions along the top wall for grid independence study.

The whole region is adopted in Fig. 4(a). At the nozzle outlet, an extended area of $25H_t \times 40H_t$ is established downstream to ensure accuracy. Upper and lower extension sections have the same area of $10H_t \times 18H_t$, which can ensure computational convergence. As displayed in Fig. 4(b-d), mesh refinement is considered for each important part. Since a series of shocks, expansion fans, and shear layers interact with each other, dense grids are essential. Owing to the gas viscosity influence, the shear layer becomes weaker and weaker from near-field to far-field. Consequently, a gradual sparse grid distribution along horizontal and vertical coordinates is reasonable. The maximum y^+ value along the top nozzle wall is 0.9. Sharp points seriously affect the computational convergence, therefore, a smooth transition mode is adopted along nozzle walls, as shown in Fig. 4(e). Pressure inlet and outlet conditions are utilized. The nozzle inlet utilizes the pressure inlet boundary. The extended domain is set as the pressure outlet. Other boundaries are set as adiabatic walls. Ansys Fluent is utilized based on a density-based solver. In the flow field, shock wave/boundary layer interaction, primary upstream vortex (PUV), and secondary upstream vortex (SUV) occur. The SST $k-\omega$ model can better predict the above phenomena (Islam *et al.* 2018a, b; Wu and Kim 2019a; Wu *et al.* 2020c). Hence, it is used. Ideal gas state equation is considered and second-order upwind schemes are adopted. The implicit formulation is used. The Advection Upstream Splitting Method (AUSM) is chosen to solve a general system of conservation equations. The stagnation temperature is $T_0 = 300\text{K}$, and the Reynolds number is $Re = 1.6 \times 10^6$.

3.4 Mesh Independence Study

As shown in Fig. 5, three grids are tested, which have 253,000 cells, 491,120 cells, and 896,500 cells. The pressure of grid 2 almost coincides with that of grid 3. The pressure of grid 1 shows some gaps

from that of grid 2 and grid 3. The GCI technology is used to quantify the error accurately (Roache 1994). Three meshes have a refinement ratio ($n = 2$). The minimum dimensionless pressure ratio, P_{uw}/P_b , upstream of the bypass outlet is taken as the convergence parameter, where $I_1 = 1.14977$ (grid 1), $I_2 = 1.1189$ (grid 2), and $I_3 = 1.1122$ (grid 3).

Firstly, the accuracy is calculated according to Eq. (18).

$$\varphi = \ln \left(\frac{I_1 - I_2}{I_2 - I_3} \right) / \ln(n) = 2.204 \quad (18)$$

The safety factor of $F_s = 1.25$ is used herein (Wu and Kim 2019a; Wu *et al.* 2020a). Then, GCI_{12} and GCI_{23} values are shown as follows:

$$GCI_{12} = \frac{F_s \left| \frac{I_2 - I_1}{I_2} \right|}{n^\varphi - 1} * 100\% = 0.956\% \quad (19)$$

$$GCI_{23} = \frac{F_s \left| \frac{I_3 - I_2}{I_3} \right|}{n^\varphi - 1} * 100\% = 0.209\% \quad (20)$$

$$\Pi = \frac{GCI_{12}}{n^\varphi \cdot GCI_{23}} = 0.993 \approx 1 \quad (21)$$

Because the coefficient Π is very close to 1, a good solution to the asymptotic convergence range is proved. Hence, a grid of 491,120 cells is selected.

4. RESULTS AND DISCUSSION

4.1 Experimental Verification

All available experimental data are quoted from the reference paper, which provides normalized total

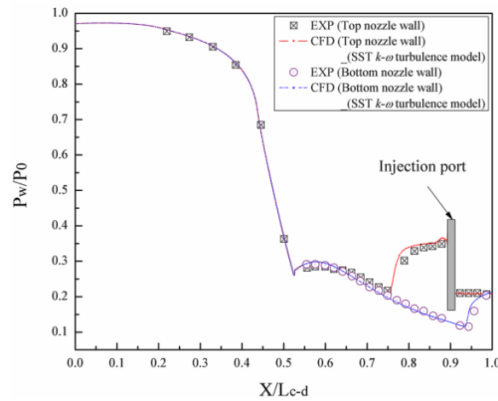


Fig. 6. Experimental validation of computational static pressures along the top and bottom walls.

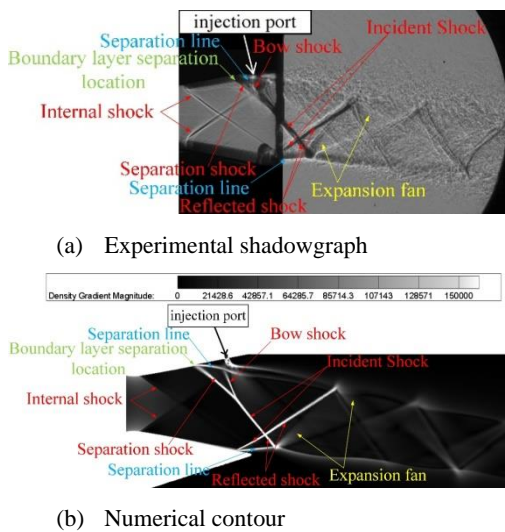


Fig. 7. Comparison between experimental shadowgraph and numerical results (a) experimental shadowgraph (Waithe and Deere 2003); (b) numerical contour.

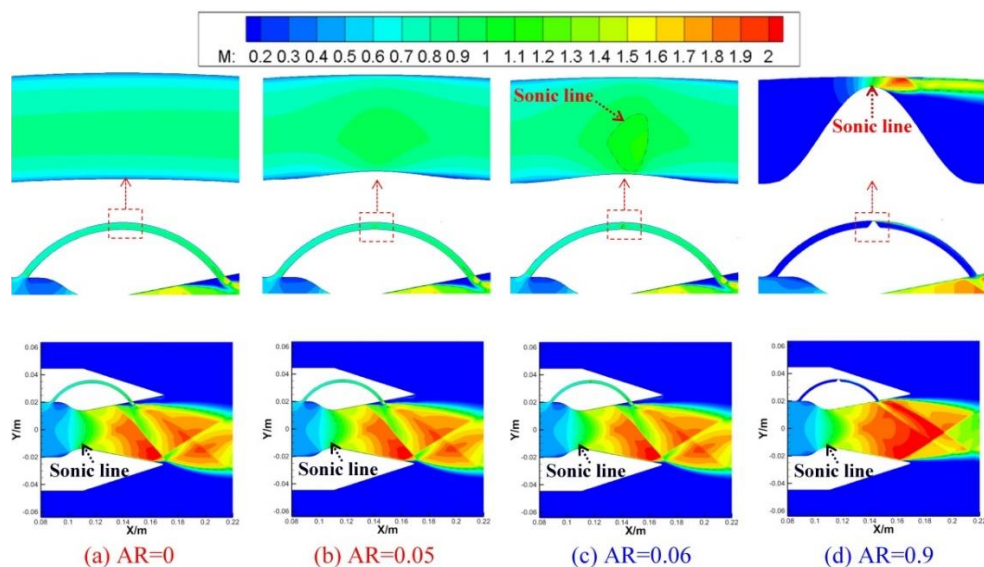


Fig. 8. Mach contours for different shrinkage area ratios of the bypass (NPR = 4.6) (a) AR = 0; (b) AR = 0.05; (c) AR = 0.06; (d) AR = 0.9.

pressure values for the top and bottom walls (Waithe and Deere 2003). The experiment was carried out at NPR = 4.6 and SPR = 3.22. Figure 6 depicts the normalized static pressure on the top wall and the bottom wall has a good consistency. Figure 7 shows the qualitative comparison between the experimental shadowgraph and the density gradient magnitude contour. It reveals that the two phenomena are almost consistent. Thus, the current numerical method is accurate.

4.2 Impact of the Bypass Shrinkage Area Ratio

Eight bypass shrinkage area ratios are analyzed for NPR = 4.6, involving AR = 0, 0.05, 0.06, 0.08, 0.1, 0.4, 0.7, and 0.9. Mach number contours are depicted in Fig. 8 to expound all flow details. The Laval nozzle is always choked. In addition, as the bypass momentum flux decreases, the jet vectoring angle decreases with the increasing shrinkage area ratio of the bypass. For AR = 0, the flow gets choked at the location of the bypass outlet because of the boundary layer impact. Flow choking has three situations, namely, friction choking, geometry choking, and thermal choking. Due to the adiabatic wall assumption without any heat transfer, thermal choking is impossible. Owing to the constant bypass area, geometry choking does not exist. The choking flow is generated at the bypass outlet. The superiority of the present arc bypass is proved here, in comparison to earlier bypass structures causing an uncertain flow choking position. As AR = 0.05, the flow in the bypass finally chokes at the bypass outlet at present because the maximum bypass shrinkage height is smaller than the boundary layer thickness. Compared with geometry choking, friction choking plays a major role. When the bypass shrinkage area ratio is AR = 0.06, the geometry choking occupies a crucial role in the bypass flow control. The flow choking appears near the bypass throat section.

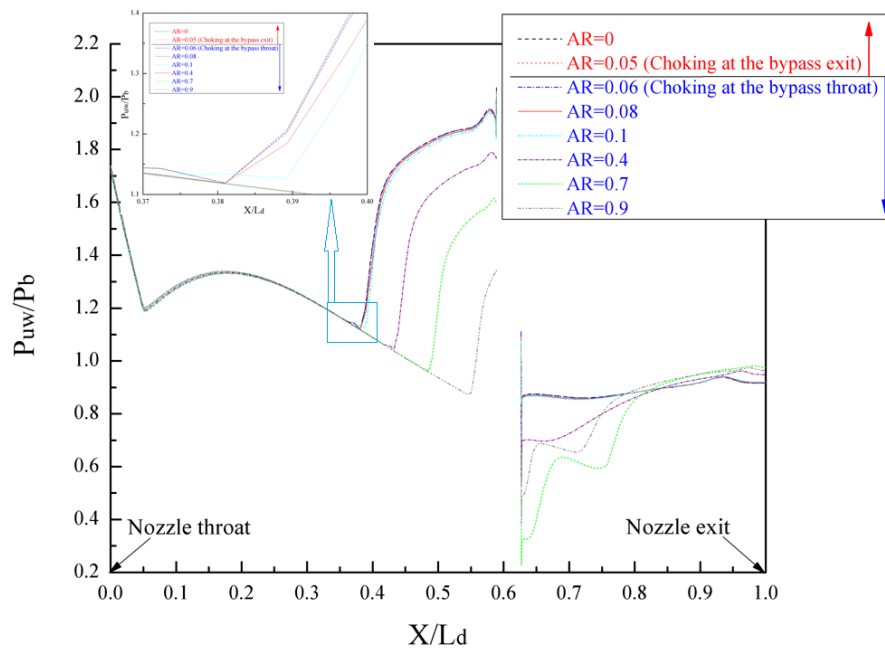


Fig. 9. Static pressure distributions along the top nozzle wall for different shrinkage area ratios of the bypass (NPR = 4.6).

When the shrinkage area ratio further increases ($AR > 0.06$), the flow choking occurs at the bypass throat because of a more significant geometry choking. Therefore, this technique can effectively modulate the flow rate to control the jet vectoring process. Figure 9 depicts static pressure distributions for diverse bypass shrinkage area ratios, in which the positions of the nozzle throat and exit are indicated. The horizontal coordinate, X/L_d , is a non-dimensionalized length ratio and the vertical coordinate, P_{uw}/P_b , is a normalized static pressure ratio. In the range of $X/L_d = 0$ to $X/L_d = 0.05$, the static pressure goes down due to the impact of expansion fans. Between $X/L_d = 0.05$ and $X/L_d = 0.2$, the static pressure rises owing to the internal shock effect (Waithe and Deere 2003). Subsequently, the sharp rise of the static pressure is due to the separation shock caused by the boundary layer separation. The separation position moves downstream with an increasing shrinkage area ratio of the bypass. Along with the sharp increase of the static pressure, a smooth pressure increase is affected by the formation of the PUV. The following pressure hump is due to the effect of the SUV. At the downstream of the bypass outlet, the pressure rise for those cases is owing to the induced shocks.

Figure 10 reveals the vectoring angles for diverse bypass shrinkage area ratios. The results indicate that the vectoring angle decreases with the increase of the shrinkage area ratio due to the diminishing momentum flux in the bypass. As the bypass flow is choked at its throat, the vectoring angle decreases rapidly with an increasing shrinkage area ratio.

Figure 11 shows the variations of bypass mass flow ratios for diverse bypass shrinkage area ratios. When the flow chokes at the bypass throat, the mass

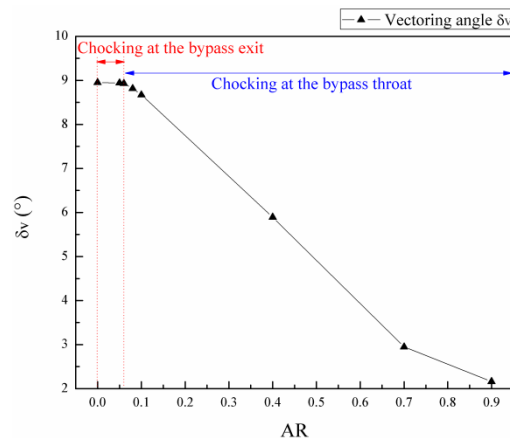


Fig. 10. Vectoring angles for different shrinkage area ratios of the bypass (NPR = 4.6).

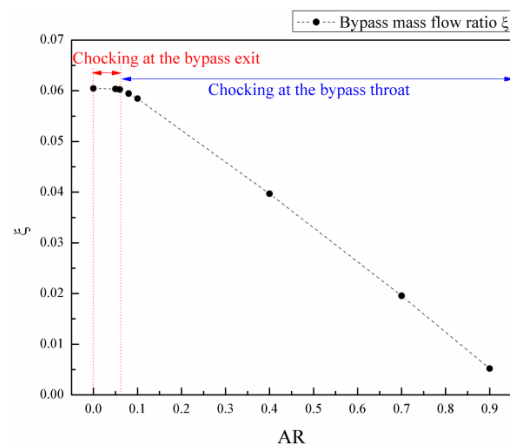


Fig. 11. Bypass mass flow ratios for different shrinkage area ratios of the bypass (NPR = 4.6).

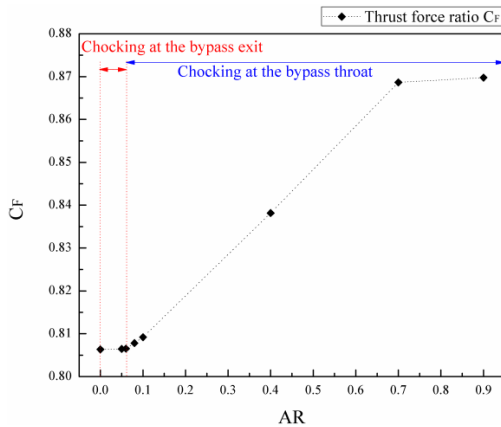


Fig. 12. Thrust force ratios for different shrinkage area ratios of the bypass (NPR = 4.6).

flow rate decreases sharply. Figure 12 depicts the thrust force ratios for diverse bypass shrinkage area ratios. The thrust force ratio continuously increases with an increasing shrinkage area ratio, since separation shocks and bow shocks become weaker. Additionally, the thrust force ratio slightly increases with the increase in shrinkage area ratio as it is related to a slight decrease in the shock loss owing to the small changes in the boundary layer separation location, PUV, and SUV. The thrust force ratio fleetly increases with an increased shrinkage area ratio since it is caused by reduced shock loss.

Figure 13 shows the variations of thrust efficiency for diverse bypass shrinkage area ratios. The thrust efficiency continues to enlarge with the increasing shrinkage area ratio. Notwithstanding that the vectoring angle constantly decreases, a faster decrease in the bypass mass flow rate results in the improvement of its efficiency. The thrust efficiency slowly increases since the shrinkage area ratio of the bypass is smaller than 0.7 and it increases dramatically after reaching AR = 0.7. Although the vectoring angle is very small for AR = 0.9, the bypass flow rate is much smaller.

The specific impulse coefficients are shown in Fig. 14 for diverse shrinkage area ratios. The specific

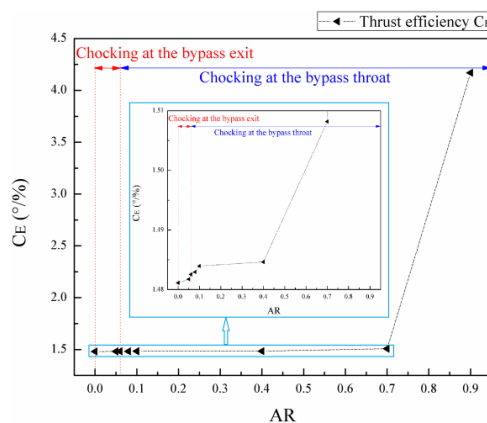


Fig. 13. Thrust efficiencies for different shrinkage area ratios of the bypass (NPR = 4.6).

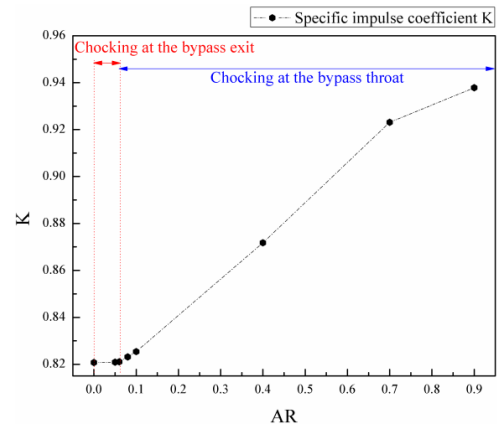


Fig. 14. Specific impulse coefficients for different shrinkage area ratios of the bypass (NPR = 4.6).

impulse coefficient increases with the increasing shrinkage area ratio. It means that generated thrust divided by the propellant mass flow rate for a higher shrinkage area ratio is more effective than that for a lower shrinkage area ratio. Figure 15 depicts the coefficients of discharge for diverse shrinkage area ratios. In all cases, the coefficient of discharge of this BSITVN is very high. The coefficient of discharge enlarges with the increasing shrinkage area ratio.

4.3 Effect of NPR

At AR = 0.4, four values involving NPR = 3, 4, 4.6, and 7 are studied to clarify the performance variations of BSITVN. Mach contours for different NPR levels are shown in Fig. 16. The sonic line demonstrates that the flow in the Laval nozzle and bypass is choked at the throat part. Moreover, the Laval nozzle changes from over-expanded conditions (NPR = 3, 4, and 4.6) to under-expanded conditions (NPR = 7). The Mach reflection occurs for NPR = 3, and a subsonic flow region appears at the back of the Mach disk and only regular reflections form in other cases.

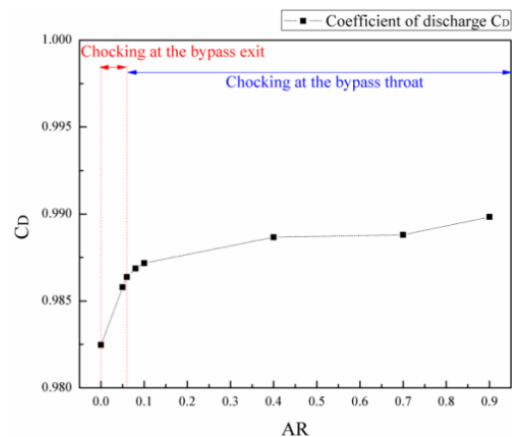


Fig. 15. Coefficients of discharge for different shrinkage area ratios of the bypass (NPR = 4.6).

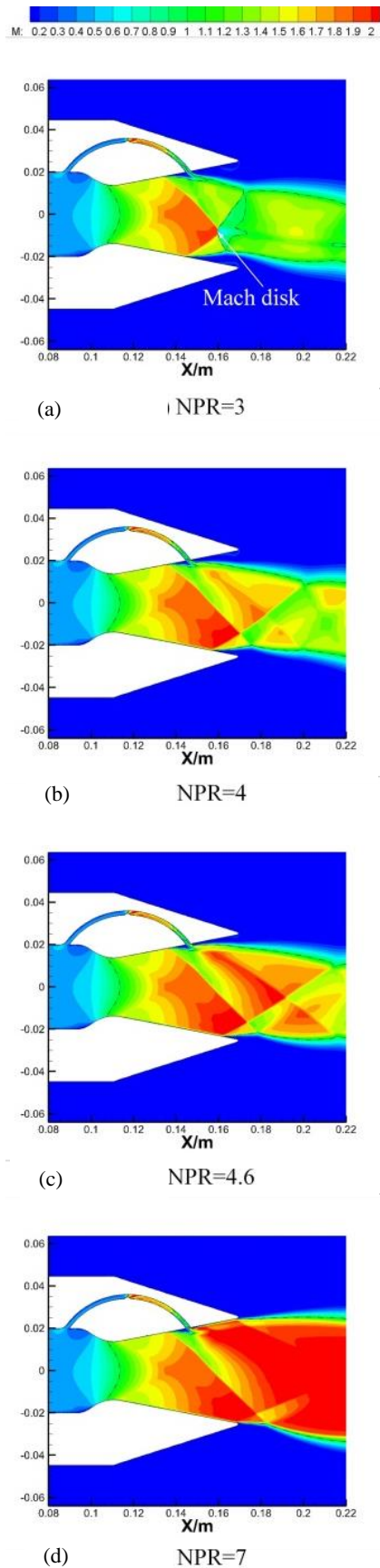


Fig. 16. Mach contours for different values of NPR (AR = 0.4) (a) NPR = 3; (b) NPR = 4; (c) NPR = 4.6; (d) NPR = 7.

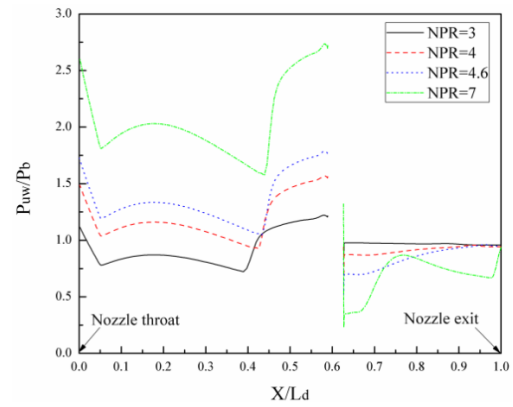


Fig. 17. Static pressure distributions along the top wall of the nozzle for different values of NPR (AR = 0.4).

Figure 17 shows the pressure distribution of the nozzle top wall for various NPR values when AR = 0.4. The corresponding streaklines are drawn in Fig. 18 to qualitatively elucidate pressure variations caused by flow separations. Since the energy stored in the gas is higher for a larger NPR level, the stronger mainstream causes the boundary layer separation to shift a little more downstream. The pressure jump at the boundary layer separation location becomes higher for a larger NPR value owing to a stronger separation shock. Beyond the sudden pressure jump, a smooth pressure rise is determined by the variation of PUV. Figure 18 shows that the area of the PUV region diminishes on and on with an increase in the NPR. The SUV region continuously diminishes with a decrease in NPR. At the downstream of the bypass outlet, a new vortex zone forms at NPR = 7, resulting in a smooth pressure variation. Subsequently, the static pressure rapidly increases due to the impact of a recompression shock. Then, the descending static pressure is owing to the flow acceleration.

Figure 19 shows vectoring angles for different values of NPR at AR = 0.4. The vectoring angle declines on and on with the increasing NPR. Because the stronger mainstream has more energy to restrain the jet deflection that is resulted from the momentum flux of the bypass flow. Figure 20 depicts thrust force ratios for diverse NPR levels. The thrust force ratio continuously increases with the increasing NPR, which is because of the diminishing thrust loss caused by multifarious shocks. It can be seen from Fig 16(a), that at NPR = 3, there are two strong oblique shocks and a normal shock in the nozzle, resulting in significant thrust loss. When the value of NPR increases, the normal shock disappears and the induced shock becomes weaker, leading to less pressure loss. The thrust efficiency continuously decreases with an increase in the level of NPR, and diverse values of NPR are shown in Fig. 21. Since the bypass mass flow ratio is invariable for different NPR values, the decreasing thrust efficiency is mainly dependent on the declining vectoring angle.

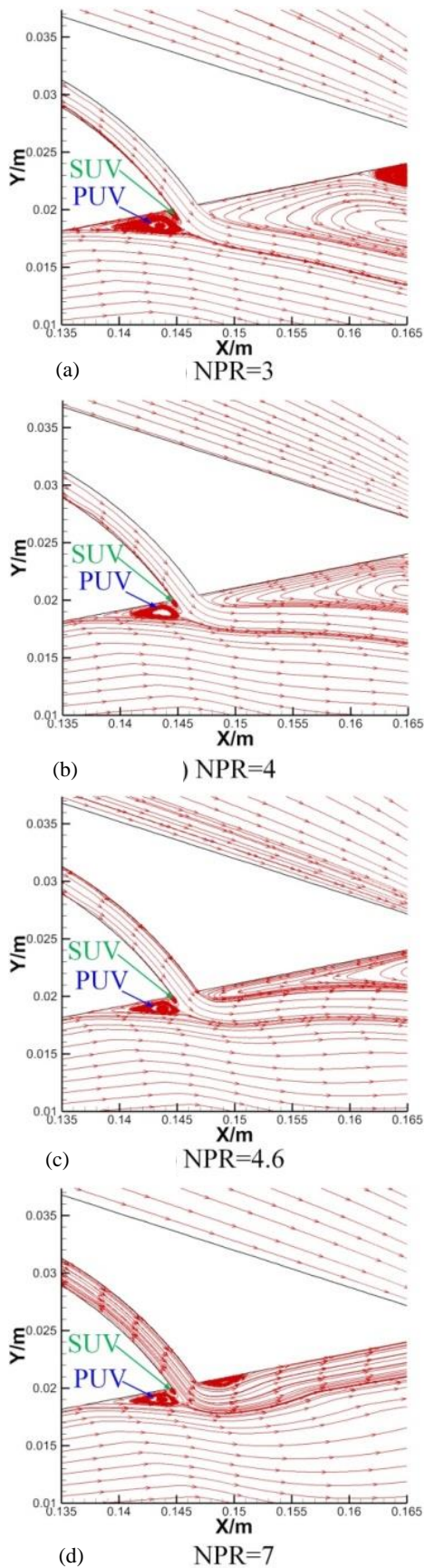


Fig. 18. Streaklines for different values of NPR (AR = 0.4) (a) NPR = 3; (b) NPR = 4; (c) NPR = 4.6; (d) NPR = 7.

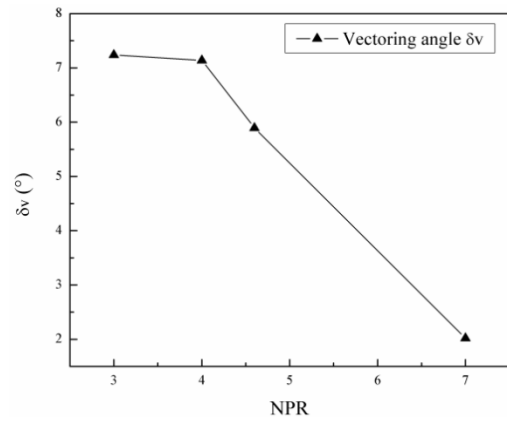


Fig. 19. Vectoring angles for different values of NPR (AR = 0.4).

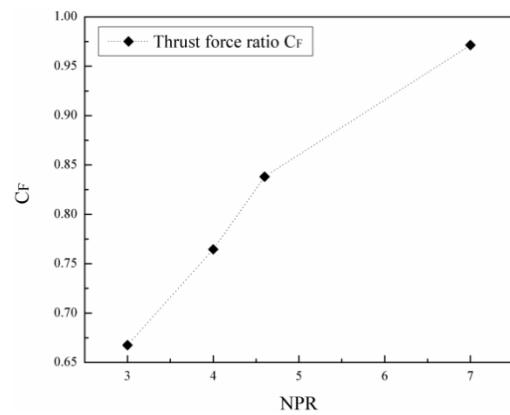


Fig. 20. Thrust force ratios for different values of NPR (AR = 0.4).

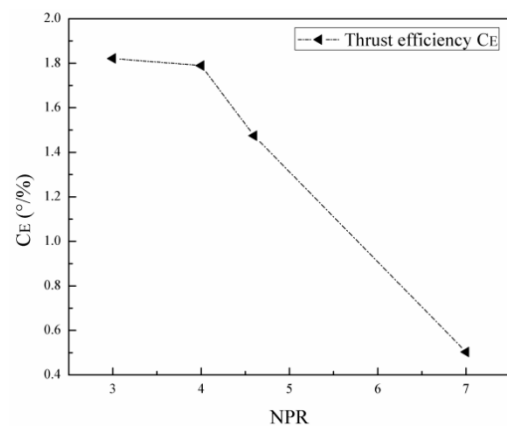


Fig. 21. Thrust efficiencies for different values of NPR (AR = 0.4).

5. CONCLUSION

The controllability of the 2-D BSITVN with an arc bypass is studied using the numerical method. The static pressure distributions give an excellent match with the experimental data, which proves the accuracy of the present computational work. With

the increase of the shrinkage area ratio, the bypass mass flow ratio reduces continuously; thrust force ratio, thrust efficiency, specific impulse ratio, and coefficient of discharge increase constantly, which testifies to the outstanding performance of the shock vectoring nozzle using an arc-shaped bypass.

This study focuses on the steady-state phenomena of BSITVN. In future work, we are going to study the 3-D BSITVN and reveal the unsteady influences in terms of the vectoring flow field along the spanwise direction, focusing on the dynamic characteristics to further reveal its physical mechanism.

ACKNOWLEDGEMENTS

The authors are grateful for the support from the National Natural Science Foundation of China (Grant No. 52206058, No. 12002241), Natural Science Foundation of Zhejiang Province (Grant No. LQ22E060002), Zhejiang Sci-Tech University Foundation (Grant No. 21022247-Y), China Postdoctoral Science Foundation (Grant No. 2020M681393), and Graduate Course Construction Project of Zhejiang Sci-Tech University (Grant No. YKC-202108).

REFERENCES

- Bhattacharya, S. and A. Ahmed (2010). Effect of sinusoidal forcing on the wake of a circular cylinder. In *48th AIAA Aerospace Sciences Meeting Including the New Horizons Forum and Aerospace Exposition*, Orlando, Florida, America.
- Bhattacharya, S. and A. Ahmed (2020). Effect of aspect ratio on the flow over a wall-mounted hemispherical turret. *International Journal of Heat and Fluid Flow* 84, 108600.
- Bhattacharya, S. and J. W. Gregory (2015a). Effect of three-dimensional plasma actuation on the wake of a circular cylinder. *AIAA Journal* 53(4), 958-967.
- Bhattacharya, S. and J. W. Gregory (2015b). Investigation of the cylinder wake under spanwise periodic forcing with a segmented plasma actuator. *Physics of Fluids* 27(1), 014102.
- Bhattacharya, S. and J. W. Gregory (2018). Optimum-wavelength forcing of a bluff body wake. *Physics of Fluids* 30(1), 015101.
- Bhattacharya, S. and J. W. Gregory (2020). The effect of spatially and temporally modulated plasma actuation on cylinder wake. *AIAA Journal* 58(9), 3808-3818.
- Burcham Jr, F. W., G. B. Gillyard and P. A. Gelhausen (1990). Integrated flight-propulsion control concepts for supersonic transport airplanes. *NASA Technique Memorandum* 101728.
- Chouicha, R., M. Sellam and S. Bergheul (2020). Effect of reacting gas on the fluidic thrust vectoring of an axisymmetric nozzle. *Propulsion and Power Research* 1-15.
- Cong, R. F., Y. D. Ye, Z. L. Zhao, J. Q. Wu and C. F. Zhang (2019). Numerical research on jet tab thrust vector nozzle aerodynamic characteristics. *Journal of Physics: Conference Series* 1300, 012089.
- Das, S. S., J. C. Páscoa, M. Trancossi and A. Dumas (2016). Computational fluid dynamic study on a novel propulsive system: ACHEON and its integration with an unmanned aerial vehicle (UAV). *Journal of Aerospace Engineering* 29(1), 04015015.
- Deere, K. A. (2003). Summary of fluidic thrust vectoring research conducted at NASA Langley Research Center. In *Proceedings of 21st AIAA Applied Aerodynamics Conference*, Orlando, Florida, America.
- Deere, K. A., B. L. Berrier, J. D. Flamm and S. K. Johnson (2003). Computational study of fluidic thrust vectoring using separation control in a nozzle. In *Proceedings of 21st AIAA Applied Aerodynamics Conference*, Orlando, Florida, America.
- Deng, R. Y. and H. D. Kim (2015). A study on the thrust vector control using a bypass flow passage. *Proceedings of the Institution of Mechanical Engineering, Part G: Journal of Aerospace Engineering* 229(9), 1722-1729.
- Deng, R. Y., T. Setoguchi and H. D. Kim (2016). Large eddy simulation of shock vector control using bypass flow passage. *International Journal of Heat and Fluid Flow* 62, 474-481.
- Ferlauto, M. and R. Marsilio (2016). Numerical simulation of fluidic thrust-vectoring. *Journal of Aerospace Science, Technology and system* 95(3), 153-162.
- Gu, R., J. Xu and S. Guo (2014). Experimental and numerical investigations of a bypass dual throat nozzle. *Journal of Engineering for Gas Turbines and Power* 136(8), 084501.
- Heo, J. Y. and H. G. Sung (2012). Fluidic thrust-vector control of supersonic jet using coflow injection. *Journal of Propulsion and Power* 28(4), 858-861.
- Islam, M. S., M. A. Hasan and A. T. Hasan (2018a). An analysis of thrust vectoring in a supersonic nozzle using bypass mass injection. In *AIP Conference Proceedings*, AIP Publishing LLC.
- Islam, M. S., M. A. Hasan, A. T. Hasan and D. Zhang (2018b). Numerical analysis of bypass mass injection on thrust vectoring of supersonic nozzle. In *MATEC Web of Conferences*, EDP Sciences.
- Joshi, K. and S. Bhattacharya (2019). Large-eddy simulation of the effect of distributed plasma forcing on the wake of a circular cylinder. *Computers and Fluids* 193, 104295.

- Kong, F. S., Y. Z. Jin and H. D. Kim (2016). Thrust vector control of supersonic nozzle flow using a moving plate. *Journal of Mechanical Science and Technology* 30(3), 1209-1216.
- Roache, P. J. (1994). Perspective: a method for uniform reporting of grid refinement studies. *Journal of Fluid Engineering* 116(3), 405-413.
- Sellam, M., Z. Vladeta, L. Leger and A. Chpoun (2015). Assessment of gas thermodynamic characteristics on fluidic thrust vectoring performance: analytical, experimental and numerical study. *International Journal of Heat and Fluid Flow* 53, 156-166.
- Sung, H. G. and Y. S. Hwang (2004). Thrust-vector characteristics of jet vanes arranged in x-formation within a shroud. *Journal of Propulsion and Power* 20(3), 501-508.
- Waite, K. A. and K. A. Deere (2003). Experimental and computational investigation of multiple injection ports in a convergent-divergent nozzle for fluidic thrust vectoring. In *Proceedings of 21st AIAA Applied Aerodynamics Conference*, Orlando, Florida, America.
- Wang, Y. S., J. L. Xu, S. Huang, Y. C. Lin and J. J. Jiang (2019). Computational study of axisymmetric divergent bypass dual throat nozzle. *Aerospace Science and Technology* 86, 177-190.
- Wu, K. X. (2022). Study on aerodynamic features of rod thrust vector control for physical applications. *Proceedings of the Institution of Mechanical Engineering, Part G: Journal of Aerospace Engineering*, 1-21.
- Wu, K. X. and H. D. Kim (2019a). Numerical study on the shock vector control in a rectangular supersonic nozzle. *Proceedings of the Institution of Mechanical Engineering, Part G: Journal of Aerospace Engineering* 233(13), 4943-4965.
- Wu, K. X. and H. D. Kim (2019b). Study on fluidic thrust vector control based on dual-throat concept. *Journal of Korean Society of Propulsion Engineers* 23(1), 24-32.
- Wu, K. X. and H. D. Kim (2019c). Fluidic thrust vector control using shock wave concept. *Journal of Korean Society of Propulsion Engineers* 23, 10-20.
- Wu, K. X. and H. D. Kim (2021). A fluidic thrust vector control using the bypass flow in a dual throat nozzle. *Journal of Mechanical Science and Technology* 35(8), 1-10.
- Wu, K. X., A. Suryan and H. D. Kim (2019a). Assessment of aerodynamic characteristics on shock vector control. *Recent Asian Research on Thermal and Fluid Sciences* 669-685.
- Wu, K. X., H. D. Kim and Y. Z. Jin (2018). Fluidic thrust vector control based on counter-flow concept. *Proceedings of the Institution of Mechanical Engineers, Part G: Journal of Aerospace Engineering* 233(4), 1412-1422.
- Wu, K. X., S. K. Raman, V. R. P. Sethuraman, G. Zhang and H. D. Kim (2020a). Effect of the wall temperature on Mach stem transformation in pseudo-steady shock wave reflections. *International Journal of Heat and Mass Transfer* 147, 118927.
- Wu, K. X., T. H. Kim and H. D. Kim (2020b). Sensitivity analysis on counter-flow thrust vector control with a three-dimensional rectangular nozzle. *Journal of Aerospace Engineering* 34(1), 04020107.
- Wu, K. X., T. H. Kim and H. D. Kim (2020c). Theoretical and numerical analyses of aerodynamic characteristics on shock vector control. *Journal of Aerospace Engineering* 33(5), 04020050.
- Wu, K. X., Y. Z. Jin and H. D. Kim (2019b). Hysteresis behaviors in counter-flow thrust vector control. *Journal of Aerospace Engineering* 32(4), 04019041.
- Yagle, P. J., D. N. Miller, K. B. Ginn and J. W. Hamstra (2001). Demonstration of fluidic throat skewing for thrust vectoring in structurally fixed nozzles. *Journal of Engineering for Gas Turbines and Power* 123(3), 502-507.
- Zmijanovic, V., L. Leger and E. Depussay (2016). Experimental-numerical parametric investigation of a rocket nozzle secondary injection thrust vectoring. *Journal of Propulsion and Power* 32(1), 196-213.
- Zmijanovic, V., L. Leger, V. Lago, M. Sellam and A. Chpoun (2012). Experimental and numerical study of thrust-vectoring effects by transverse gas injection into a propulsive axisymmetric C-D nozzle. In *Proceedings of 48th AIAA/ASME/SAE/ASEE Joint Propulsion Conference*, Atlanta, Georgia, America.
- Zmijanovic, V., V. Lago and A. Chpoun (2014). Thrust shock vector control of an axisymmetric conical supersonic nozzle via secondary transverse gas injection. *Shock Waves* 24(1), 97-111.
- Zou, X. H. and Q. Wang (2011). The comparative analysis of two typical fluidic thrust vectoring exhaust nozzles on aerodynamic characteristics. *International Journal of Aerospace and Mechanical Engineering* 5(4), 827-833.
- Zucker, R. D. and O. Biblarz (2002). *Fundamentals of Gas Dynamics*. Wiley, America.